applied sciences

MDPI

Article

HIT Solar Cell Modeling Using Graphene as a Transparent Conductive Layer Considering the Atacama Desert Solar Spectrum

Henrry Revollo [1,*], Pablo Ferrada [2,*], Pablo Martin [1], Aitor Marzo [3] and Valeria del Campo [4,5]

[1] Departamento de Física, Universidad de Antofagasta, Av. Angamos 601, Antofagasta 1270300, Chile; pablo.martin@uantof.cl
[2] Centro de Desarrollo Energético Antofagasta, Universidad de Antofagasta, Av. Angamos 601, Antofagasta 1270300, Chile
[3] Department of Optics, Faculty of Science, University of Granada, 18071 Granada, Spain; aitorm@ugr.es
[4] Departamento de Física, Universidad Técnica Federico Santa María, Av. España 1680, Valparaíso 2390123, Chile; valeria.delcampo@usm.cl
[5] Millenium Nucleus in NanoBioPhysics (NNBP), Av. España 1680, Valparaíso 2390123, Chile
* Correspondence: henrry.revollo@ua.cl (H.R.); pablo.ferrada.m@uantof.cl (P.F.); Tel.: +56-55-2-513-645 (H.R.)

Abstract: The optical and geometrical properties of transparent conductive oxide (TCO) are crucial factors influencing the efficiency of a $-$ Si : H/c $-$ Si heterojunction (HIT) solar cells. Graphene is a potential candidate to be used as TCO due to its optical and electrical properties. Here, the effect of graphene as TCO is numerically analyzed by varying the number of graphene layers from one to ten. First, the optical properties are calculated based on the transmittance data, and then the HJT cell's performance is simulated under the AM1.5 standard spectrum and the mean Atacama Desert solar spectral irradiance in Chile. In the modeling, the most relevant properties are calculated with the spectrum of the Atacama Desert. The most relevant values were obtained as follows: open circuit voltage $V_{oc} = 721.4$ mV, short circuit current $J_{sc} = 39.6$ mA/cm^2, fill factor $FF = 76.5\%$, and energy conversion efficiency $E_{ff} = 21.6\%$. The maximum power of solar panels irradiated with the Atacama Desert spectrum exceeds the results obtained with the AM1.5 standard spectrum by 10%. When graphene is the transparent conducting oxide, quantum efficiency has a higher value in the ultraviolet range, which shows that it may be convenient to use graphene-based solar cells in places where ultraviolet intensity is high.

Keywords: HIT solar cell; Atacama Desert; solar spectral irradiance; graphene; AFORS-HET

Citation: Revollo, H.; Ferrada, P.; Martin, P.; Marzo, A.; del Campo, V. HIT Solar Cell Modeling Using Graphene as a Transparent Conductive Layer Considering the Atacama Desert Solar Spectrum. *Appl. Sci.* **2023**, *13*, 9323. https://doi.org/10.3390/app13169323

Received: 10 July 2023
Revised: 5 August 2023
Accepted: 7 August 2023
Published: 17 August 2023

1. Introduction

Heterojunction with intrinsic thin layer (HIT) solar cells based on silicon $a - Si : H/c - Si$ have reached efficiencies above 26% [1]. Interface quality and transport properties are the critical HIT solar cell factors for energy conversion [2]. Thus, several studies focus their efforts to improve the performance of $a - Si : H/c - Si$ HIT solar cells by optimizing the quality of the interface and enhancing their transport properties [1–3].

The transparent conductive layer (TCL) is the layer responsible for separating and transporting photogenerated charge carriers to the cell terminals. This is due to the formation of a Schottky barrier in the electrode-silicon interface. At the same time, the TCL acts as an antiretive layer of internal reflections [1–3]. Thus, TCL must have low surface resistance and high optical transmission. Indium tin oxide, one of the TCLs that is most used, has a resistance of ~20 Ω/sq, with 85% optical transmission and a high carrier mobility of 160 cm^2/V·s [1–6].

In the last few years, two-dimensional nanomaterials, such as graphene, dichalcogenides (such as WS_2), and Xenes (silicene, for example), have shown potential for several

applications, such as drug delivery, sensing, energy storage, and transistors, among others [7,8]. Regarding photovoltaics, several authors have reported on the use of thin films and graphene for solar cell applications, both experimentally and based on simulations.

In perovskite solar cells, Qin et al. [9] simulated, through the SCAPS program, the incorporation of a layer of copper oxide (CuO) with voids, and analyzed the influence on the energy bands and on the electrical properties of the solar cell. They optimized the design by varying the CuO thickness and the CuO doping concentration. With the optimization, they showed an increment in the conversion factor of 5.95%.

In the study of Hora et al. [10], a layer composed of PEDOT:PSS (PP) and graphene nanoplatelets (GNP) was studied as a counter electrode. They deposited it on FTO-coated glass and on bare glass, which served as substrates for the counter electrodes. The PP plate sample exhibited higher energy conversion than the sample that had PP:GNP when using the AM1.5 solar spectrum. Conversely, when using artificial light, the sample with the PP:GNP layer showed a higher energy conversion compared to the PP plate.

Lai et al. [11] presented a metamaterial absorber based on surface plasmon resonance (SPR). The structure consisted of (Graphene /SiO_2/Au) matrix, and the simulation was conducted with COMSOL software. The absorber could achieve triple-mode perfect absorption, polarization independence, incident angle insensitivity, tunability, high sensitivity, and a high figure of merit (FOM). In Tang et al. [12], the researchers demonstrated that the polarization-controlled multiple plasmon-induced transparency (PIT) depends on the symmetry in a graphene-based meta surface. The unit cell of the meta surface was composed of two U-shaped graphene nanostructures and one ring-shaped graphene nanostructure that is deposited on a dielectric substrate. For this study, they modeled through the finite time difference method, and they varied the configuration of the nanostructure. For each configuration, the maximum transition happens for different frequencies.

Graphene has shown an interesting potential as a transparent conductor in several optoelectronic devices, such as LED, solar cells, touch screens, and so on [13,14]. Danietti et al. [15] studied the incorporation of graphene as a transparent conductive layer in organic cells. For this purpose, they also included a Niquel grid below the graphene layer to enhance electrical conductivity. With this configuration, the efficiency of the organic cell was 4.2%, which was lower compared to the use of ITO (6.1%) due to a higher sheet resistance. Graphene has also been studied for ITO and AZO replacement in HIT cells due to its high transparency (97% for the monolayer) [16,17]; for its sheet resistance, which is as low as 0.882 Ω/cm^2 [6]; and for its carrier mobility, which is over 7350 $cm^2/V{\cdot}s$ [18–20]. Lancellotti et al. [21] characterized the sheet resistance, varying the number of graphene layers between one and five, and with only four and five layers, they achieved AZO conductivity properties. Thus, they tested the HIT cells with four and five graphene layers instead of AZO as the transparent conductive layer. With both numbers of layers, they obtained similar results, with efficiencies between 8.6% and 9.95%, while the efficiency with AZO was 15.21%. Torres et al. [22] were able to increase the efficiency of a HIT cell by including a graphene monolayer on top of the ITO film of the cell. However, the addition of more layers decreased optical transmittance, and it resulted in a poorer performance compared to bare ITO.

Since a HIT solar cell involves many processing variables, such as donor concentration, acceptors, layer thickness, transparent conductive oxide (TCO) film deposition, metallic electrodes, etc., experimentally examining the effect of each variable on the performance of the cell is a huge task. Thus, numerical simulation has become almost essential for understanding and designing solar cells. Automat for Simulation of Heterostructure (AFORS-HET) software was developed by a team at Berlin Hahn–Meitner Institute, and it is used for simulating heterojunction solar cells [23]. AFORS-HET is convenient for assessing and optimizing the different parameters (thickness, doping concentration, forbidden band, resistivity, etc.) present in the manufacturing of HIT solar cells [24,25].

Although graphene has great potential for photovoltaics, there are few simulation studies regarding the replacement of standard transparent conductive layers (such as ITO

or AZO) with this nanomaterial [26,27]. Most reports simplify the structure of the cell, and they use graphene to form a Schottky junction. Additionally, to the best of our knowledge, only illumination under standard conditions or artificial light has been considered. In this work, first we optimized the structural and electrical parameters of a bifacial Si-HIT cell structure: ITO/a − Si : H(p type)/a − Si : H(i − type)/c − Si : H(n − type)/a − Si : H(i − type)/a − Si : H(n^+ − type)/ITO, evaluating the thickness and the doping of the base, the emitter, and the back surface field. This optimization was performed under two spectra, AM1.5 and the Atacama spectra. Thus, we obtained two different optimized structures for SHJ cells depending on the incident spectrum. The front ITO was then replaced by graphene as the front TCL, simulating the effect for each optimized structure under the corresponding spectrum and varying the number of graphene layers from 1 to 10.

2. Materials and Methods

2.1. Atacama Desert Solar Spectrum

Spectral irradiance is a key parameter for estimating the performance of solar cells, since their response is spectrally dependent on incident radiation. The spectral distribution of solar radiation depends on the characteristics of the gas and aerosol mixture that make up the local atmosphere, and it also depends on the length of the path that is travelled by the light, which is related to the air mass. These local characteristics may largely vary over time and from one place to another, thereby giving the solar spectrum a different form [28–30].

The reference standard spectrum G173 [31] was calculated according to the North American geographic and atmospheric conditions and a resulting air mass of 1.5 [32,33]. These conditions may differ greatly from those found in other geographical regions of the world.

In 2018, the mean solar spectrum of the Atacama Desert [34] was calculated from the spatio-temporal means of long-term databases for local atmospheric parameters. The databases contained satellite and model retrieval data from MODIS [35,36] and AIRS [37], provided by Era Interim [38,39] and Giovanni [40] for the Atacama Desert area located in Chilean territory and covering longitudes from 60 W to 85 W and latitudes from 10 S to 40 S. To replicate the methodology that was used to calculate the standard spectrum G173, we used SMARTS radiative atmospheric transfer code [39,41] and the spatio-temporal means of the atmospheric parameters of the Atacama Desert, such as aerosol optical depth (AOD) at 550 nm corrected for land, precipitable water (PW), ozone total column (TOC), relative humidity (RH), albedo, and atmospheric temperature. The consulted databases cover 10 years from January 2006 to January 2016. To validate the methodology, several points of the estimated spectral irradiance were compared with ground spectral solar irradiance measurements. The results showed that the difference between the simulation and the measurements was within the uncertainty of the instrument, with a maximum relative error of 3%. Additionally, the 18° sloping surface facing the sun was chosen to represent the average latitude of the Atacama Desert between 13° S and 30° S. Finally, the mean air mass at noon was calculated for the same latitudes, resulting in 1.08 mean air mass (AM1.08). (For more details, see [34].)

Thus, the Atacama Desert's mean solar spectra was obtained using a methodology similar to the referential standard spectrum [34].

The main characteristic of the Atacama Desert average spectrum is its blue shift with respect to the standard G173 reference spectrum, as shown in Figure 1. The scarce presence of ozone and atmospheric aerosols leads to higher levels of irradiance in the short wavelength, the ultraviolet, and the visible spectral ranges, exceeding by 55% the ultraviolet irradiance of the standard reference spectrum [34].

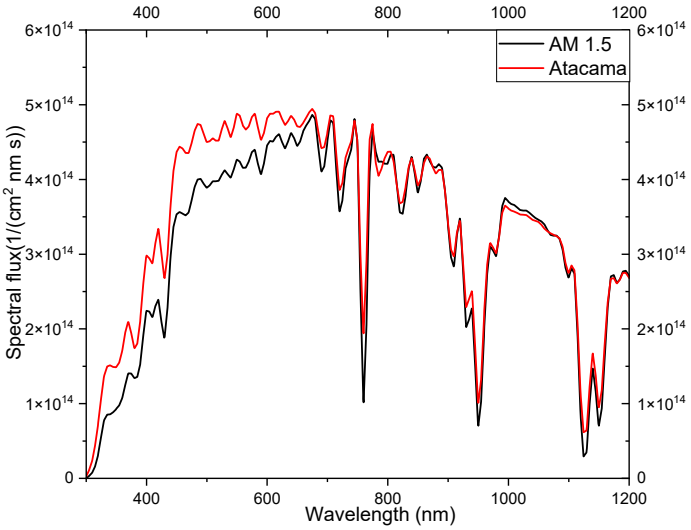

Figure 1. The black line shows the standard G173 reference spectrum with a 1.5 air mass (AM1.5). The red line shows the spectrum calculated for the Atacama Desert. Both are normalized to 1000 W m^{-2} [34].

2.2. Optical Properties of Graphene

This paper studies the use of graphene as a transparent conductive oxide on the front layer of the solar cell. To assess the impact of the proposal on the performance of the cell, the optical properties resulting from considering different graphene layers (from one to ten layers) are modelled. The optical properties calculated for graphene are refractive index (n), reflectance (R), and absorbance (A). The thickness of each layer of graphene is 0.34 nm [42]. Figure 2a shows the diagram of graphene layers on the substrate. Figure 2b shows the spectral transmittance, $T(\lambda)$, of the considered graphene layers, and the values are obtained from refractiveindex.info database [43].

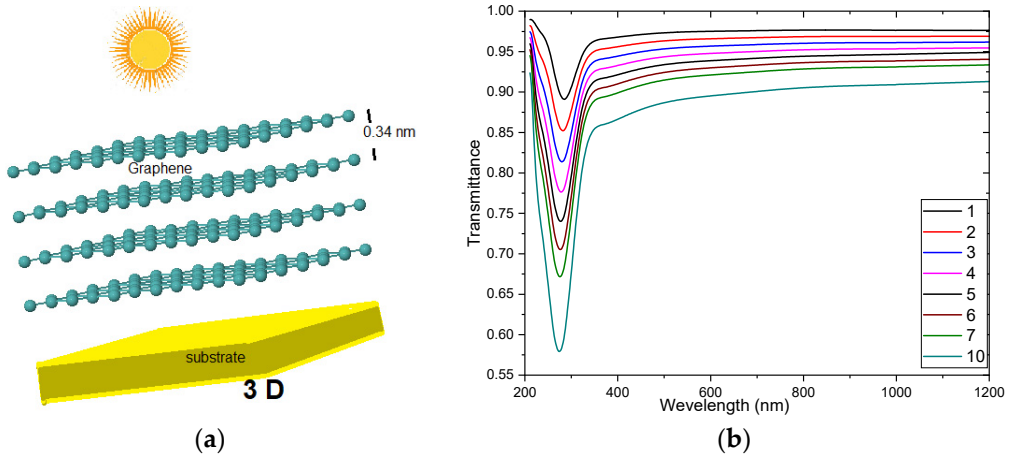

(**a**) (**b**)

Figure 2. (**a**) Graphene layers on the glass substrate. (**b**) Transmittance graph from refractiveindex.info database.

Absorbance $A(\lambda)$ is calculated with Equation (1), where the wavelength is in nm [36]:

$$A(\lambda) = \log\left(\frac{1}{T(\lambda)}\right), \tag{1}$$

Extinction coefficient $k(\lambda)$ is calculated in terms of absorption, according to Equation (2) [44]:

$$k(\lambda) = 2.303\frac{A(\lambda)}{4\pi d}, \tag{2}$$

where d is the sample thickness of graphene in nm. The complex refractive index of graphene is calculated by optimizing the transmittance expressed as $T_{cal} = T(s(\lambda),\ n(\lambda),\ k(\lambda), d)$, which depends on the substrate refraction index $s(\lambda)$, the graphene refraction index $n(\lambda)$, the graphene extinction coefficient $k(\lambda)$, and the thickness d. To do this, the approximate transmittance $T_{apx}(\lambda, d)$ and T_{cal} are minimized [44]:

$$minimized \sum_{\lambda} \left[T_{apx}(\lambda, d) - T_{cal}(s(\lambda),\ n(\lambda),\ k(\lambda), d)\right]^2 \tag{3}$$

where $T_{apx}(\lambda, d) = T(\lambda) - \Delta T$ is detailed in Equation (4) according to the refractiveindex.info database, with $T(\lambda)$ as shown in Figure 2b and the correction factor, ΔT, being the approximation function that changes according to the wavelength range obtained by approximating the experimental values of $n(\lambda)$ [42]:

$$T_{apx}\ (\lambda, d) = \begin{cases} T(\lambda) - (0.0003\lambda - 0.0578), & 210 < \lambda < 270 \\ T(\lambda) + (0.0002\lambda - 0.0701), & 271 < \lambda < 348 \\ T(\lambda) + \left(5 * 10^{-6}\lambda - 0.0039\right), & 349 < \lambda < 532 \\ T(\lambda) + \left(9 * 10^{-7}\lambda - 0.0020\right), & 533 < \lambda < 1200 \end{cases} \tag{4}$$

To calculate the refractive index, non-linear equations are solved numerically using Equation (5) [44,45]:

$$T_{cal}\ (s(\lambda),\ n(\lambda),\ k(\lambda), d) = \frac{Ax}{B - Cx + Dx^2} \tag{5}$$

where

$$\begin{aligned} A &= 16s\left(n^2 + k^2\right) \\ B &= \left[(n+1)^2 + k^2\right]\left[(n+1)\left(n + s^2\right) + k^2\right] \\ C &= \left[\left(n^2 - 1 + k^2\right)\left(n^2 - s^2 + k^2\right) - 2k^2\left(s^2 + 1\right)\right]2cos\varphi \\ &\quad -k\left[2\left(n^2 - s^2 + k^2\right) + \left(n^2 + 1\right)\left(n^2 - 1 + k^2\right)\right]2sin\varphi \\ D &= \left[(n-1)^2 + k^2\right]\left[(n-1)\left(n - s^2\right) + k^2\right] \\ \varphi &= \tfrac{4\pi nd}{\lambda}, \qquad x = e^{-\alpha d}, \qquad \alpha = \tfrac{4\pi k}{\lambda} \end{aligned}$$

The substrate corresponds to glass, so the substrate refraction index, $s(\lambda)$, is given by Equation (6) [36,37]:

$$s(\lambda) = \sqrt{1 + (0.7568 - 7930/\lambda^2)^{-1}} \tag{6}$$

Equations (1)–(6) were used to calculate the refractive index and the extinction coefficient, obtaining values similar to those reported by Weber [42]. Figure 3 shows $n(\lambda)$ and $k(\lambda)$ for the graphene from the monolayer up to ten layers.

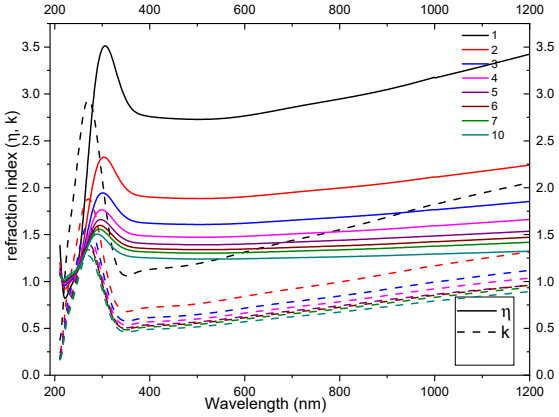

Figure 3. Solid lines show the refraction index $n(\lambda)$. Dashed lines show the extinction coefficient $k(\lambda)$. Color lines show the number of layers.

2.3. Resistive Properties of Graphene

In HIT solar cells, it is difficult to evaluate the contribution of series resistance (R_s) to their performance [46,47]. Contacts between amorphous doped layers and transparent conductive oxides are the main electrical barriers for both electrons and holes [46,47]. Some authors report the series resistance of HIT solar cells ranging from 0.1 Ω cm^2 to 0.7 Ω cm^2 [24,25] depending on several variables, such as contact geometry, ITO tin concentration, temperature, etc. This study for the solar cell with ITO uses $R_s = 0.3\ \Omega$ cm^2 based on [48,49].

When the main contribution to R_s comes from the series resistance of the front transparent conductive layer, the relation between R_s and the sheet resistance of the TCO material is given by Equation (7) [46]:

$$R_s = \frac{1}{12} R_{sh} \frac{(s - w_f)}{l_f} as \tag{7}$$

where s is finger spacing distance; w_f is finger width; l_f finger length; and a is unit cell busbar length, having the same approximations $s \sim 0.2$, $w_f \sim 0.01$, $l_f \sim 3.8$, and $a \sim 3$, measured in cm. Measuring the sheet resistance (R_{sh}) of graphene is still complicated [50–52] as it depends on several parameters, such as the substrate [50–54], the doping that graphene has [55–57], the wavelength [57], and the transmittance [50,57–59]. Due to the complexity in this article, values collected from some of the other articles on this subject will be used. The black line in Figure 4 are the sheet resistance values for n graphene layers, and the red dot is the value used to calculate the series resistance, as shown in Figure 4.

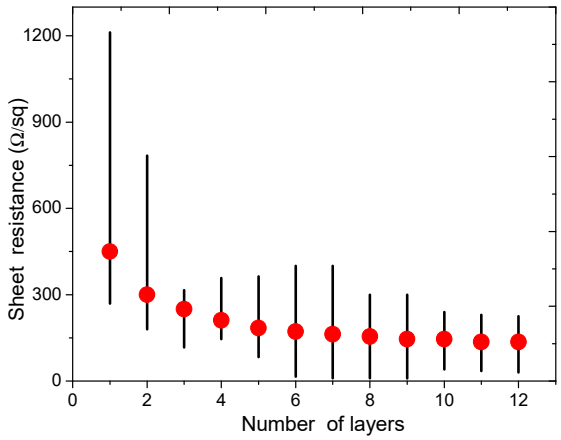

Figure 4. Graphene sheet resistance according to the number of layers, compiled from the literature [50–59].

2.4. Data

This study uses the optical properties included in AFORS-HET for the layers of amorphous silicon $(a-Si)$, crystalline silicon $(c-Si)$, indium tin oxide (ITO), and AM1.5 standard spectrum. The HIT structure is built with the electric properties and carrier/hole density shown in Table 1. The values shown in Table 1 are previously optimized for the $Gr/a-Si:H(p)/a-Si:H(i)/c-Si:H(n)/a-Si:H(i)/a-Si:H(n^+)$/ITO structure shown in Figure 5 at 1.5 air mass (AM1.5) illuminations and 100 mW/cm^2 power density.

Table 1. Parameter range of crystalline and amorphous graphene silicon materials.

Input Parameters	a-Si:H(n+)	a-Si:H(i)	a-Si:H(p+)	c-Si:H(n)
Thickness (nm)	3–12	4	3–12	$(10-20)\times10^4$
Dielectric constant dk	11.9	11.9	11.9	11.9
Electron affinity χ (eV)	3.8	3.8	3.8	4.05
Band gap E_g (eV)	1.74	1.74	1.7	1.12
Effective conduction band density N_c (cm^{-3})	1×10^{20}	1×10^{20}	1×10^{20}	2.8×10^{19}
Effective valence band density N_v (cm^{-3})	1×10^{20}	1×10^{20}	1×10^{20}	1.04×10^{19}
Electron mobility μ_n $(cm^2\ V^{-1}s^{-1})$	10	20	10	1040
Hole mobility μ_p $(cm^2\ V^{-1}s^{-1})$	1	2	1	421
Doping concentration of acceptors N_a (cm^{-3})	0	0	$(6.05-6.30)\times10^{17}$	0
Doping concentration of donors N_d (cm^{-3})	$(1-3)\times10^{18}$	0	0	$(4-14)\times10^{16}$
Thermal velocity of electrons v_e $(cm\ s^{-1})$	1×10^7	1×10^7	1×10^7	1×10^7
Thermal velocity of holes v_h $(cm\ s^{-1})$	1×10^7	1×10^7	1×10^7	1×10^7
Layer density ϱ (gcm^{-3})	2.328	2.328	2.328	2.328
Auger recombination coefficient for electron $(cm^6\ s^{-1})$	0	0	0	2.2×10^{-31}
Auger recombination coefficient for hole $(cm^6\ s^{-1})$	0	0	0	9.9×10^{-32}
Direct band-to-band recombination coefficient $(cm^3\ s^{-1})$	0	0	0	9.9×10^{-32}

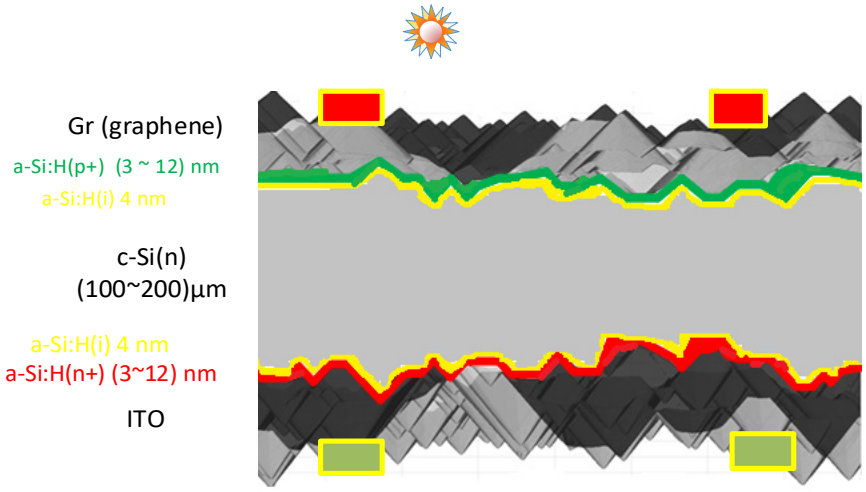

Figure 5. Solar cell schematic model in this work $Gr/a-Si:H(p)/a-Si:H(i)/c-Si:H(n)/a-Si:H(i)/a-Si:H(n^+)/ITO$.

2.4.1. Data Calculation

The Atacama Desert solar spectrum was estimated from spatio-temporal averages of long-term satellite and model retrieval databases of local environmental parameters, according to Marzo [31]. The optical properties of graphene are calculated according to Equations (2)–(6) from the transmittance data in [44].

2.4.2. Geometrical Properties

Contact parameters are shown in Table 2. The front contact is the positive pole, while back contact is the negative one, as shown in Figure 5. The metal-semiconductor interface is determined by the MS–Schottky numerical model, and the interface between the conductors is given by the drift-diffusion model, with the spacing between the semiconductor wafers being 1 .

Table 2. Front and back contact parameters.

Contact Parameters	Front Contact	Back Contact
Width (nm)	3.4–34.0	70
File	#Gr.nk	ITO.nk
Metal work function	3.0 eV	Yes (flatband)
Absorption loss	#Gr.abs	ITO.abs
External reflection constant	#Gr.ref	aSicSi_ITO.ref
Surface condition	Textured	Textured
Internal reflection constant	0	0

Solar cell modeling also considers the metallization of the front and back parts. The geometrical characteristics of the busbars and the fingers are shown in Table 3 [60,61].

Table 3. Front and back metallization parameters.

Metallization Parameters	Fingers		Busbars	
	Front	Back	Front	Back
Number	120	120	5	5
Height (µm)	30	30	30	30
Width (µm)	45	45	500	500
Cell area [cm^2]	244.315			

As reference, this study considers the approximate experimental values of the heterojunction solar cell $a-Si:H/c-Si$: open-circuit voltage $V_{oc} = 713$ mV, short-circuit current density $J_{sc} = 37.3\ mA/cm^2$, fill factor $FF = 75.9\%$, and energy conversion efficiency $\eta = 20.2\%$, as measured by Muñoz et al. in their study [62,63].

3. Results and Discussion

This study optimizes the main electrical properties of the HIT solar cell from its physical and geometrical modeling and compares the calculated efficiencies when the cell is irradiated from the back η_{back} and front η_{front} sides. Bifaciality is defined by $B_f = \eta_{back}/\eta_{front}$, with both efficiencies calculated under the same conditions. The front and back surfaces show a pyramidal structure in the plane direction $c-Si\ \langle 111 \rangle$. Series resistance in the solar cell is $0.3\ \Omega\ cm^2$ when the front transparent conductor oxide is ITO. To optimize the solar cell, the AM1.5 standard spectrum and the solar spectrum determined for the Atacama Desert were used. Here, calculations were made at a temperature of 300 K. The geometrical structure order is $ITO/a-Si:H(p^+)/a-Si:H(i)/c-Si(n)/\ a-Si:H(i)/a-Si:H(p^+)/ITO$ from the front layer to the back one.

3.1. Optimization by Changing the Carrier Concentration

During the modeling, first light impinges on one side of the cell while the other is completely dark and then it does so the other way around, and bifaciality (B_f) is computed. The I-V curve is calculated varying the carriers' concentration in each layer, and the electrical properties are recorded. Figures A1–A3 in the Appendix A show the open circuit voltage (V_{oc}), short circuit current density (J_{sc}), fill factor (FF), and energy conversion efficiency (E_{ff}) as a function of $c-Si(n)$ donor concentration (Figure A1), $a-Si:H(p^+)$ acceptor concentration (Figure A2), and $a-Si:H(n^+)$ donor concentration (Figure A3) for the Standard and Atacama Desert spectra.

Figure A1 shows the optimization of the crystalline silicon layer $c-Si(n)$ when donor concentration ranges are between $0.4 \times 10^{17}\ 1/cm^3$ and $1.4 \times 10^{17}\ 1/cm^3$. When the light impinges on the back side, the current density reaches the highest value, $J_{sc} = 34.88\ mA/cm^2$, for a donor concentration of $9.5 \times 10^{16}\ 1/cm^3$ (red circle in Figure A1a). When the light hits from the front, the J_{SC} increases its value as the concentration of donors increases, and, in the modeling, it is not possible to infinitely increase the donors be-

cause this leads to the Fermi energy level (E_f) being lower than the conduction energy E_c in the $c-Si$ shell, which is not possible [17]. However, if the carrier concentration is $>0.4 \times 10^{17}$ 1/cm^3 in the $c-Si$ layer concentration, this corresponds to $J_{sc} = 34.86$ mA/cm^2. The V_{oc} curve tends to decay with increasing donor concentration when the light strikes on the back and front parts. Bifaciality comes closer to 1 when reducing the concentration. Additionally, the energy conversion efficiency and the fill factor reach the highest value at a low concentration. For Atacama Desert solar spectral irradiance, when modeling is performed considering the fact that the light strikes the back side of the cell, the current density reaches the highest value, $J_{sc} = 34.86$ mA/cm^2, at a concentration of 10×10^{16} 1/cm^3.

The optimum donor concentration is chosen to be the one that maximizes the short current density, which in Figure 5 is marked with a red circle for both spectra because the modeling is performed separately and independently when (i.) the light falls from the front and (ii.) when the light falls from behind.

The electrical characteristics of the $p-type$ hydrogenated amorphous silicon layer are very important for HIT solar cells. Figure A2 shows the $a-Si : H(p^+)$ hydrogenated amorphous silicon layer optimization with $p-type$ carriers varying between $(6.05-6.30) \times 10^{17}$ 1/cm^3. In the modeling, most parameters increase with the number of carriers. However, for large concentrations, the Fermi energy level of the acceptors (E_f) reaches higher values than the valence energy levels (E_v), which is physically not possible. For AM1.5 solar spectral irradiance, bifaciality reaches the highest value for a concentration of 6.22×10^{17} 1/cm^3, where it is marked with the red circle. When modeling is performed under the Atacama spectrum, bifaciality reaches the highest value for 6.28×10^{17} 1/cm^3, marked with a red circle in Figure A2. Values of V_{oc} tend to increase at a higher acceptor concentration in the studied range, and short-circuit current density remains constant. Energy conversion efficiency and the fill factor of the two spectra studied tend to increase with concentration.

Figure A3 shows the optimization of the hydrogenated amorphous silicon layer $a-Si : H(n^+)$ varying donors between $(1.0-3.0) \times 10^{18}$ 1/cm^3 above this range $Efn < Ec$ in the $a-Si{:}(n^+)$ layer. Bifaciality comes closer to 1 at a higher donor concentration. The open-circuit voltage and the short-circuit current show a small initial increment followed by a constant value with increasingly higher donor concentration. Thus, for this study, when modeling under the standard spectrum, the chosen donor concentration is 1.2×10^{18} 1/cm^3, which is marked with the red circle in the bifaciality curve. When modeling with the Atacama spectrum, the chosen concentration is 1.4×10^{18} 1/cm^3. Energy conversion efficiency and the fill factor tend to remain constant at a higher donor concentration in the studied range.

3.2. Optimization by Changing the Cell's Layers' Thickness

The layer thickness (w) plays a very important role in the optimization of the material, but, at the same time, it is extremely important to have an optimized thickness to achieve the highest energy conversion efficiency. This process can be carried out in the laboratory by varying the manufacturing time or the intensity of the gas flow [51,52].

Figure A4 in the Appendix A shows the optimization of the n^+ $(a-Si : H\ n^+)$ hydrogenated amorphous silicon layer for thicknesses varying between $(3-12) \times 10^{-7}$ cm. Here, bifaciality comes closer to 1 at a smaller thickness. The open-circuit voltage and the short-circuit current density are constant in the simulation when the light strikes the front part of the solar cell, but they decrease as the thickness increases when modeling with the light striking from the back part of the solar cell. The fill factor is constant when the light strikes from the front part, but it has a slight decay of thickness when the light strikes from the back part. The electrical properties show constant values when the light strikes from the front part. Thus, the n^+ layer thickness does not play an important role in HIT solar cells when the light strikes only from the front part, but if the light strikes from the back side, the n^+ layer thickness is quite relevant.

We denote the edge of the conduction band by (E_c). Bandshifts (ΔE_c) are present at each $a-Si:H(i)/a-Si:H(n)$ interface. If the thickness of the $n-type$ layer decreases $\Delta E_c = w^{-1/2}$, this calculation is not reflected directly from J_{sc} in Figure A4. The FF is shown where the two curves have the same value, and we therefore choose the value of the thickness where it is marked with the red circle. Under AM1.5 standard spectrum, the n^+ layer is fixed at 7 nm, while under the Atacama Desert spectrum, it is fixed at 9 nm.

Figure A5 in Appendix A shows the optimization of the $type\ p^+\ a-Si:H(p^+)$ hydrogenated amorphous silicon layer for thicknesses varying between $(3-12)\times 10^{-7}$cm, showing that bifaciality is closer to 1 at a larger thickness. The open-circuit voltage values increase with thickness while the fill factor and the energy conversion efficiency decrease as the layer thickness increases. The short-circuit current density decreases as the thickness (w) increases if light strikes from the front part, while it remains constant if the light strikes from the back side. The cell behavior is similar when modeling with AM1.5 standard spectrum or Atacama Desert light intensity. In the $a-\mathrm{Si(p)}/a-\mathrm{Si(i)}$ interface, ΔE_c has a potential behavior of the form $\Delta E_c = w^{1/2}$. Under the AM1.5 standard spectrum, for $w = 6$ nm, ΔE_c presents the depletion zone in $a-Si:H(p)$, which is reflected in the bifacial curve approaching 1 above $w = 6$ nm. The fill factor has the same value regardless of the illuminated size. On the other hand, for $w = 7$ nm, the J_{sc} and the FF are reflected under the Atacama Desert spectrum.

Figure A6 in Appendix A shows the optimization of the $n\ c-Si(n)$ crystalline silicon wafer with thicknesses varying between $(120-200)\times 10^{-4}$ cm, which shows that bifaciality comes closer to 1 as thickness decreases. The open-circuit voltage tends to decrease as thickness increases. The short-circuit current density values increase as thickness increases when the light strikes from the front part. When modeling with the standard spectrum and light striking from the back part, the short-circuit current density reaches its highest value, i.e., 160×10^{-4} cm, so this is the chosen thickness for the $c-Si$ wafer under the AM1.5 standard spectrum. When modeling with Atacama Desert irradiance spectrum and light striking from the back part, the highest short-circuit current density is obtained for 150×10^{-4} cm, so this is the chosen value for Atacama spectrum. The fill factor and the energy conversion efficiency decrease as thickness increases. When the light strikes from the back part, η decreases faster.

Figure A7 in Appendix A shows the modeling of the $a-Si:H(i)$ intrinsic layer, which is located between the $a-Si:H(n^+)$ and the $c-Si$ layers. Bifaciality comes closer to 1 for a lower thickness of this layer. The open-circuit voltage is constant for $(1-5)$ nm thickness when modeling is performed considering that the light strikes the front and the back parts. The short-circuit current density is constant if the light strikes from the front, but if the light strikes from the back side, J_{sc} tends to decrease as thickness increases. In addition, the fill factor and the energy conversion efficiency tend to decrease as the thickness increases when light impinges from the back side. Here, 5 nm thickness was chosen for the intrinsic layer of the back part for the two spectra.

The $a-Si:H(i)$ intrinsic layer, located between $a-Si:H(p^+)$ and $c-Si$, is also modelled and shown in Figure A8 (see Appendix A). Here, J_{sc} tends to decrease slightly in the $(1-5)$ nm thickness range. The open-circuit voltage decreases in the studied range with a larger slope when the light strikes from the back part. The fill factor remains constant when the light strikes from the back and the front sides. Thus, the thickness of the intrinsic layer located between *p-type* and n-*type* layers is fixed at 4 nm.

3.3. Optimized Parameters

3.3.1. Generation and Recombination with AM1.5, and Atacama Spectrum

The optical model used in this work is from Lambert-Beer, where the generation of carriers $G(\lambda)$ is calculated by integrating the radiation flux $\Phi_0(\lambda)$, by $R(\lambda)$, $A(\lambda)$, and $\alpha(\lambda)$ in the wavelength [46], and Figure 6 shows that the generation of carriers with the AM1.5 standard spectrum is lower compared to the generation rate modeled with the Atacama spectrum. In Figure 6, it can also be seen that the carrier recombination rate does not

depend on $\Phi_0(\lambda)$. The direct dependence of the generation of carriers with the radiation flux $G(\lambda) \propto \Phi_0(\lambda)$ makes the HIT heterojunction solar cell have a better energy conversion performance in places such as the Atacama Desert.

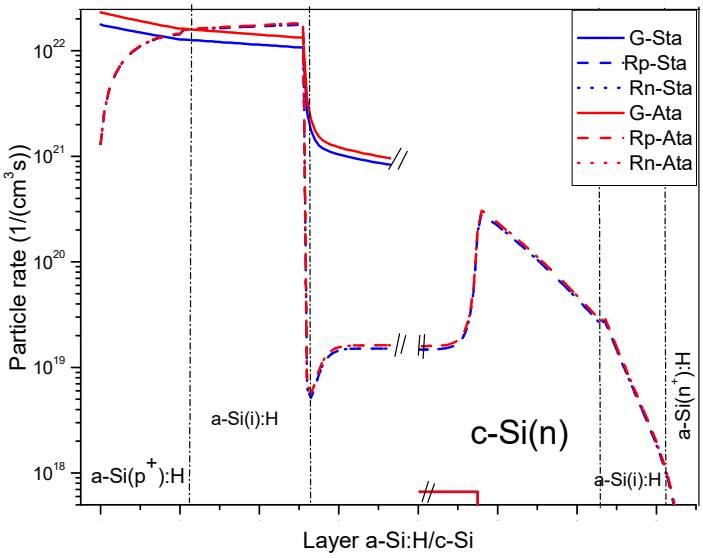

Figure 6. Generation and recombination with AM1.5 and Atacama spectrum in the five layers of the HIT solar cell.

3.3.2. Optimization of the Solar Cell with ITO as TCO

Through the modeling previously performed, the optimal parameters, summarized in Table 4, were obtained for each spectrum. The comparison between $AM1.5/op$ and Ata/op solar cells shows that the solar cell for the Atacama Desert should have the $c-Si(n)$ layer $\approx 6\%$ thinner, the $a-Si:H(p^+)$ layer 16% thicker, and the layer of $c-Si(n)$ with a lower concentration of minority carriers.

Table 4. Electrical characteristics of solar cells.

Parameter	V_{oc} [mV]	J_{sc} [mAcm^{-2}]	*FF* [%]	*Eff* [%]
AM1.5/op	761.9	37.19	76.88	21.78
Ata/op	763.9	40.82	76.49	23.85

With these parameters, the electrical properties are obtained by calculating the current density curve as a function of voltage under the standard AM1.5 ($AM1.5/op$) and under the Atacama Desert (Ata/op) spectra (Figure 7). Table 5 shows the main characteristics of the solar cell under each spectrum.

Table 5. Electrical parameter of the HIT solar cell.

Parameter/Spectrum	AM1.5	Atacama	Unit
Nd_c − Si(n)	9.5×10^{16}	10×10^{16}	cm^{-3}
Na_a − Si(p^+)	6.24×10^{17}	6.28×10^{17}	cm^{-3}
Nd_a − Si(n^+)	1.2×10^{18}	1.4×10^{18}	cm^{-3}
w_a − Si(n^+)	7	9	Nm
w_a − Si(p^+)	6	7	Nm
w_c − Si(n)	160	150	Nm
w_a − Si(i) − p	4	4	Nm
w_a − Si(i) − n	5	5	Nm

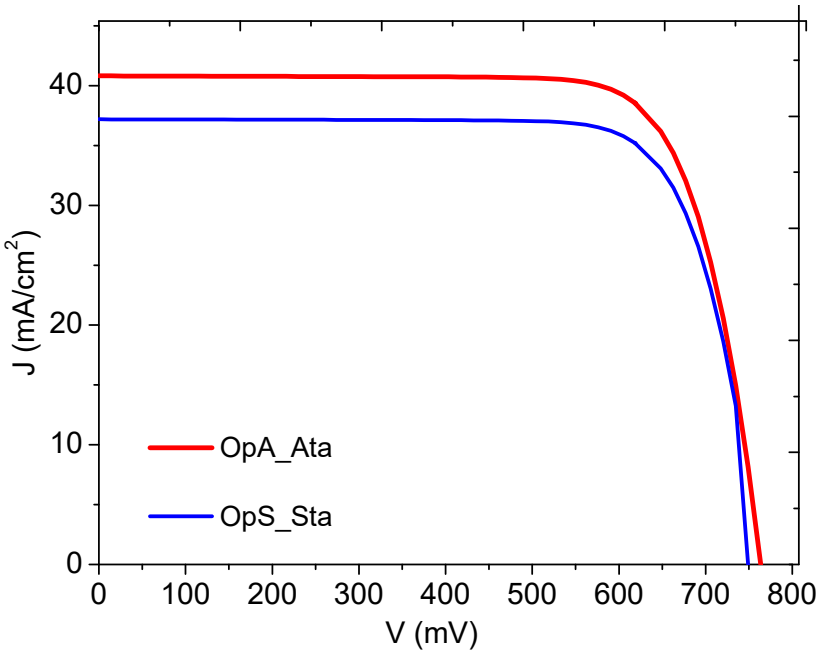

Figure 7. The blue line is the J-V curve of AM1.5/op. The red line is the Ata/op J-V curve values.

The optimized cell under the standard spectrum has an efficiency of 21.78%, which is 1.58 percentual points higher than the experimental result. The main difference between the experimental cell and the computed cell is in the open circuit voltage, which is 761.9 mV and 713 mV, respectively. Conversely, the short-circuit current density is 0.1 mA/cm^2 larger for the laboratory cell. When the simulation is performed considering the Atacama spectrum and the cell parameters optimized for it, the short-circuit current has an increment of 3.63 mA/cm^2 compared to the AM1.5 simulation. This is the main cause of the larger efficiency under the Atacama spectrum compared to the standard conditions.

3.3.3. Optimization of the Solar Cell Incorporating Graphene as TCO

After the HIT solar cell optimization for the standard and the Atacama spectra, the effect of replacing ITO with graphene is computed, with the aim of optimizing the number of graphene layers for each spectrum. Thus, the modeling is performed using the cell's parameters of Table 5. In this work, graphene is considered to have a 3-dimensional nature, and each layer has a thickness of a 0.34 nm. Graphene's optical properties, such as refraction index and extinction coefficient, are shown in Figure 3. The series resistance (Rs) for graphene is calculated using Equation (7) and the sheet resistance values shown in Figure 4. The obtained series resistance as a function of graphene layers is presented in Figure A9 (see the Appendix A). In this simulation, we also consider the resistance in series and the resistance in parallel, and we make it tend to infinity.

Figure A9 shows the electrical properties of the solar cell simulated with graphene instead of ITO. The open-circuit voltage curves for the AM1.5 standard spectrum and the Atacama Desert solar spectrum are similar, decreasing as the number of graphene layers increases. The short-circuit current density decreases as the number of graphene layers increases, reaching the maximum value when there is only one layer, as shown in Figure A9. Conversely, the fill factor increases as the number of graphene layers increases. These behaviours of J_{SC} and FF are expected, since graphene's transmittance decreases with the number of layers while its resistance increases. In all, the energy conversion efficiency reaches the highest value for three graphene layers, and 18.8% and 20.1% for the standard and the Atacama spectrum, respectively. These obtained efficiencies with graphene are ~10% lower than those computed with ITO. To understand this result, we calculated the optical properties and the external quantum efficiency of the HIT cell with both ITO and graphene.

3.4. Reflectance, Absorbance, Transmitance and External Quantum Efficiency

The optical properties of the HIT solar cell and its external quantum efficiency are calculated using the cell's parameters as shown in Table 5. Figure 8 shows the absorbance spectrum (Abs) in red, the reflectance (Refl) spectrum of the front side in black, the transmittance (Tras) spectrum in blue, and the external quantum efficiency (EQE) in green. The solid lines are the values calculated when the transparent conductive layer is ITO, while the dashed lines correspond to one graphene layer as a transparent conductive layer. The cell with graphene as TCO has a larger reflectance in the 300–1200 nm wavelength range, so the cell's absorbance is lower. Transmittance is the same in the whole range, regardless of which transparent electrode is being analyzed. Regarding the EQE in the ultraviolet range, the values calculated with graphene are higher than the values calculated with ITO, and in the visible range, the values calculated with ITO are higher than the values calculated with graphene. In the infrared range, they have the same value.

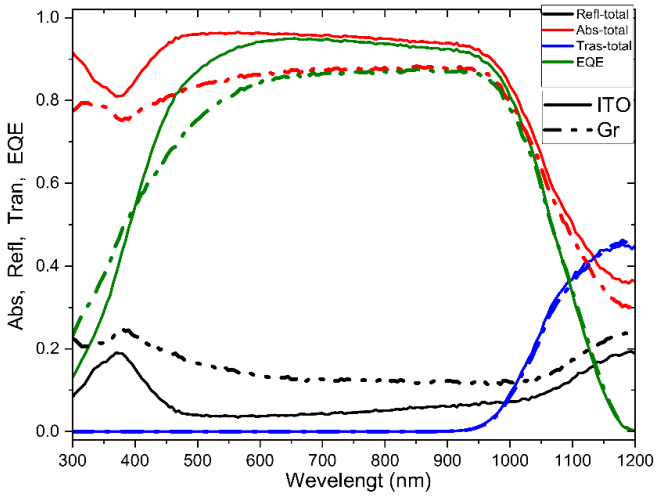

Figure 8. Reflectance, absorbance, transmittance, and external quantum efficiency. The solid line indicates that TCO is ITO. The dashed lines indicate that TCO is graphene.

3.5. Optimizing the Solar Cell with the Busbar Number

As graphene has conductive properties and is located between the semiconductor and the busbars in the cell, we consider that it can benefit the collection of carriers. For this purpose, a minimodule with one HIT cell (15.675 cm side) encapsulated with EVA rubber and glass is considered in the modeling. The busbars are 30 µm height and 540 µm width. The considered values for graphene's series resistance are those shown in Figure A9. Metallization modeling is conducted with SunSolve software [64] on a 244.315 cm^2 solar cell as well as the busbar area.

Figure A10 in the Appendix A shows the solar cell modeling with ITO and with one graphene layer instead of ITO, using the cell's values shown in Table 3. Here, the solar cell is modelled, varying the number of busbars from 2 to 10. Figure A10 shows that the efficiency increases with the number of busbars, with a limit of five busbars. As the number of busbars increases, J_{sc} and V_{oc} show a slight decay due to larger shade on the cell. However, the addition of busbars (at least up to ten) raises both the fill factor and the efficiency of the minimodule.

4. Conclusions

Heterojunction with intrinsic thin layer cells was optimized to operate under the AM1.5 standard spectrum and the Atacama Desert spectrum, varying the thicknesses and number of carriers in the different layers, and the resulting characteristics for each layer are shown in Table 5. The results show that when modeling under the Atacama spectrum, an

optimized cell has a higher efficiency than under the AM1.5 spectrum, with a percentage difference of 6.89% (the absolute values are shown in Table 4).

For the modeling of graphene as transparent conductive film, the number of graphene layers was varied from 1 to 10 layers. Under both spectra, the optimum number is three graphene layers, achieving efficiencies of 18.8% and 20.1% for the Standard and the Atacama spectra, respectively. However, the use of graphene instead of ITO decreased the efficiency of the cell in 13% for AM1.5. A similar result was obtained in the experimental work of Danietti et al. [15]: they reported a decay of 30% when they used a graphene layer with a Niquel grid instead of ITO in organic cells. A similar decay was obtained in the experiment of Lancellotti et al. [21], who used several graphene layers as AZO replacement in HIT cells. Their best result was achieved for four and five graphene layers, but the efficiencies were ~35% lower compared to the use of AZO. Torres et al. [22] deposited graphene on top of the ITO film in HIT cells and obtained an increment of 1.6% after the deposition of one graphene layer, while the addition of more layers resulted in a poorer performance compared to bare ITO.

The contribution that graphene can make to the cell with the busbars was estimated, varying the number of busbars in the square solar cell of 244.315 cm^2, and the modeling showed us that for more than seven busbars, there were cells of greater efficiency.

Although the deposition of graphene on the $a-Si:H(p)$ emitter gave lower values of the electrical characteristics, the results are still encouraging when analyzing the results of the quantum efficiency in the range of the ultraviolet spectrum, and this may have relevance to spectra such as the Atacama Desert spectrum or the extraterrestrial spectra. When graphene is the transparent conducting electrode, quantum efficiency has a higher value in the ultraviolet range, which shows that it may be convenient to use graphene-based solar cells in places where ultraviolet intensity is high.

Author Contributions: Conceptualization, P.F.; methodology, H.R. and P.F.; software, H.R. and P.F.; validation, H.R. and P.F.; formal analysis, H.R. and P.F; investigation, H.R. and P.F; resources, P.F.; data curation, H.R.; writing—original draft preparation, H.R.; writing—review and editing, P.F., P.M., A.M. and V.C; visualization, H.R.; supervision, P.F., P.M., A.M. and V.d.C.; project administration, P.F.; funding acquisition, P.F. All authors have read and agreed to the published version of the manuscript.

Funding: This research was founded by ANID/FONDECYT/11190289 project, as well as ANID/FONDAP/1522A0006 "Solar Energy Research Center, SERC-Chile"; ANID–Fondecyt 1210490; ANID–ECOS210038–C21E08 and ANID—Millennium Science Initiative Program—NNBP # NCN2021_021. In addition, we recognize the support of the Graduate School at the Universidad de Antofagasta. A. Marzo would like to thank the Ramon y Cajal contract (RYC2021-031958-I), funded by the Spanish Ministerio de Ciencia e Innovación MCIN/AEI/10.13039/501100011033 and by the European Union "NextGenerationEU/PRTR".

Institutional Review Board Statement: Not applicable.

Informed Consent Statement: Not applicable.

Data Availability Statement: Data available on request.

Acknowledgments: We recognize the support of Helmholtz-Zentrum Berlin for providing the AFORS-HET simulation software.

Conflicts of Interest: The authors declare no conflict of interest.

Appendix A

Referred figures in the Results and Discussion section are place in the Appendix.

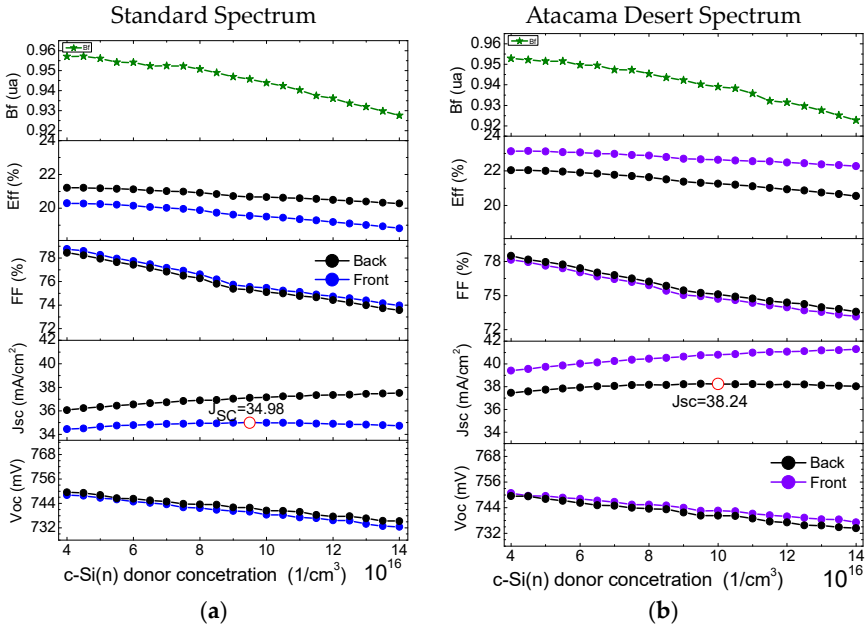

Figure A1. $c - Si(n)$ optimization, according to donor concentration. (**a**) The black line shows bifaciality and IV values when the light strikes the back part, while the blue line shows these values when the light strikes the front part, with the AM1.5 standard spectrum. (**b**) The black line shows bifaciality and IV values when the light strikes the back part, while the violet line shows these values when the light strikes the front part, with the Atacama Desert solar spectrum.

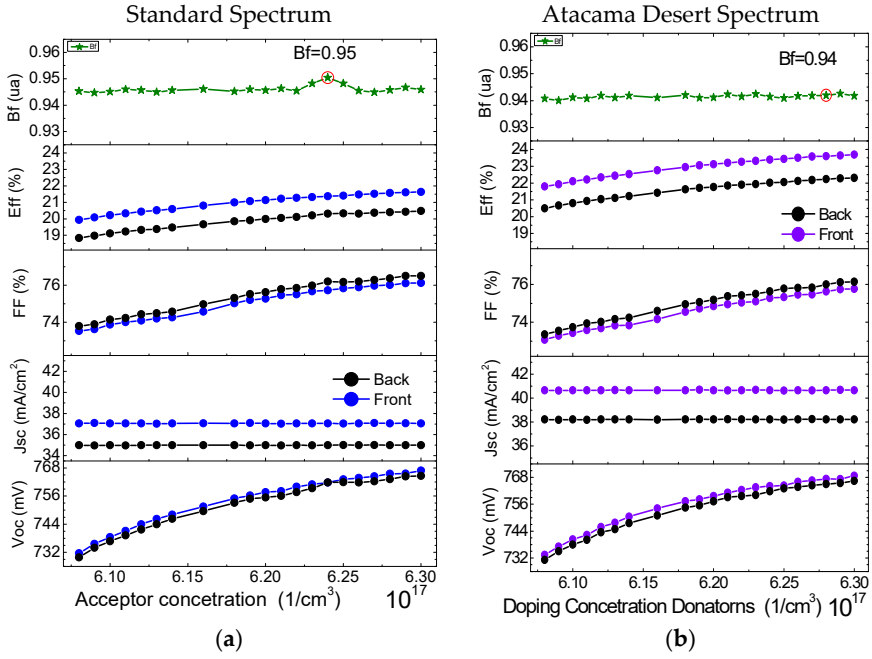

Figure A2. $a - Si : H(p^{+})$ optimization, according to acceptor concentration. (**a**) The black line shows bifaciality and IV values when the light strikes the back part, while the blue line shows these values when the light strikes the front part, with the AM1.5 standard spectrum. (**b**) The black line shows bifaciality and IV values when the light strikes the back part, while the violet line shows these values when the light strikes the front part, with the Atacama Desert solar spectrum.

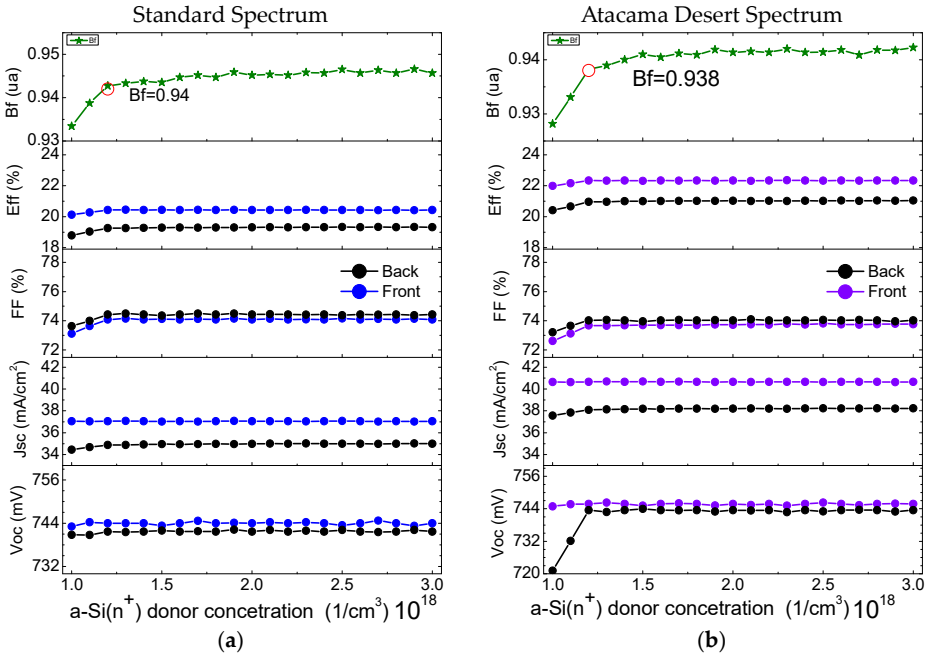

Figure A3. $a-Si:H(n^{+})$ optimization, according to donor concentration. (**a**) The black line shows bifaciality and IV values when light strikes the back part, while the blue line shows these values when the light intensity strikes the front part, with the AM1.5 standard spectrum. (**b**) The black line shows bifaciality and IV values when the light strikes the back part, while the violet line shows these values when the light intensity strikes the front part, with the Atacama Desert solar spectrum.

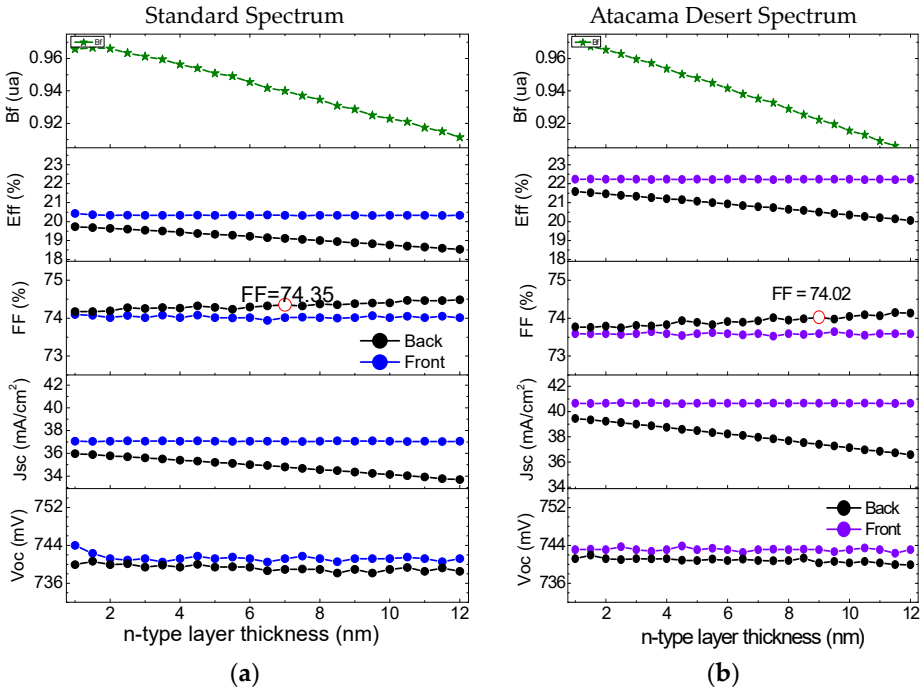

Figure A4. $a-Si:H(n^{+})$ optimization, according to thickness. (**a**) The black line shows bifaciality and IV values when the light strikes from the back part, while the blue line shows these values when the light strikes from the front part, with the AM1.5 standard spectrum. (**b**) The black line shows bifaciality and IV values when the light strikes from the back part, while the violet line shows these values when the light strikes with the front part, with the Atacama Desert spectrum.

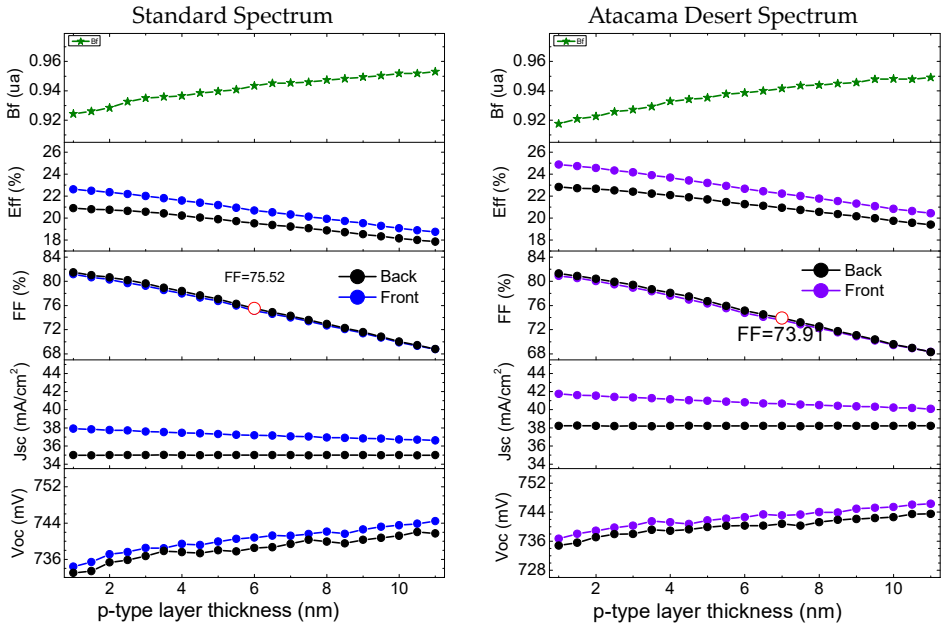

Figure A5. $a-Si:H(p^{+})$ optimization, according to thickness. (**a**) The black line shows bifaciality and IV values when the light strikes from the back part, while the blue line shows these values when the light strikes from the front part, with AM1.5 standard spectrum. (**b**) The black line shows bifaciality and IV values when the light strikes from the back part, while the violet line shows these values when the light strikes from the front part, with Atacama Desert spectrum.

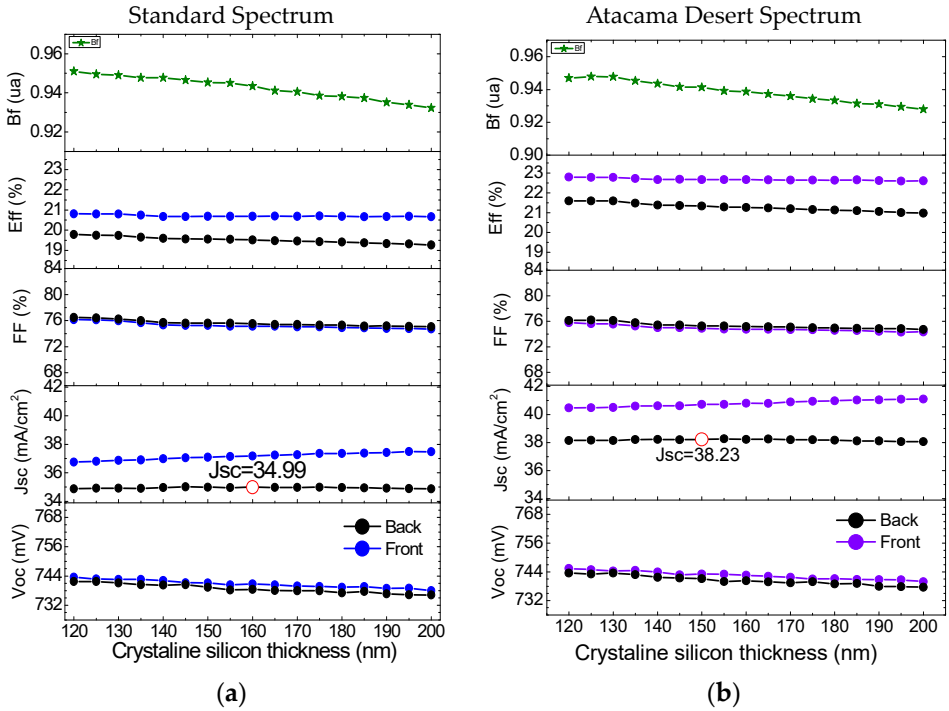

Figure A6. $c-Si(n)$, according to function. (**a**) The black line shows bifaciality and IV values when the light strikes from the back part, while the blue line shows these values when the light strikes from the front part, with AM1.5 standard spectrum. (**b**) the black line shows bifaciality and IV values when the light strikes from the back part, while the violet line shows these values when the light strikes from the front part, with Atacama Desert solar spectrum.

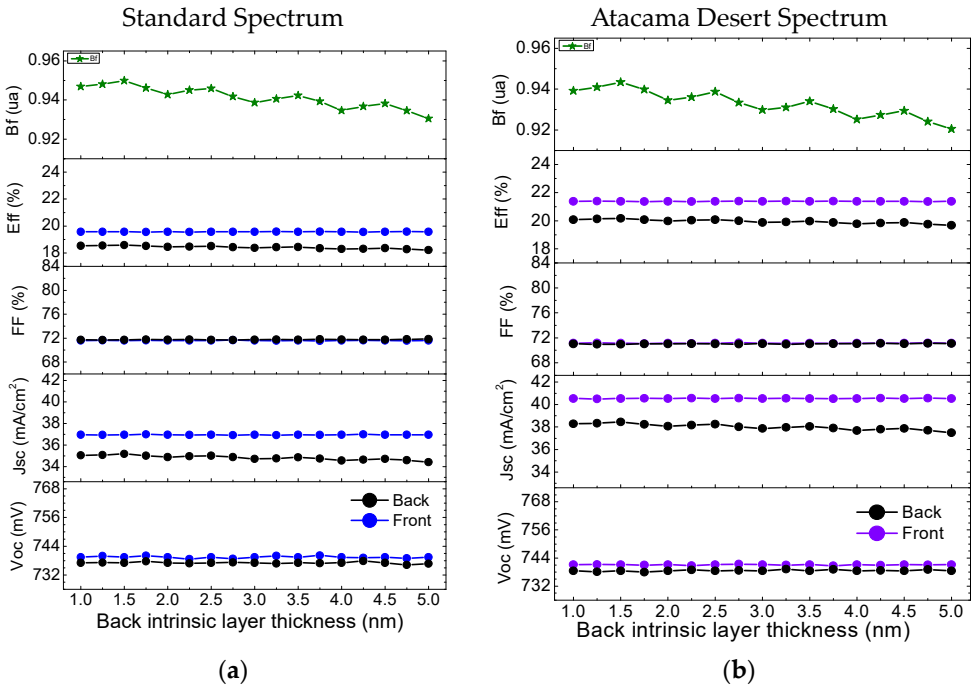

Figure A7. Optimization of $a - Si : H(i)$ at the back part of the solar cell, according to thickness. (**a**) The black line shows bifaciality and IV values when the light strikes from the back part, while the blue line shows these values when the light strikes from the front part, with the AM1.5 standard spectrum. (**b**) The black line shows bifaciality and IV values when the light strikes from the back part; while the violet line shows these values when the light strikes from the front part, with the Atacama Desert solar spectrum.

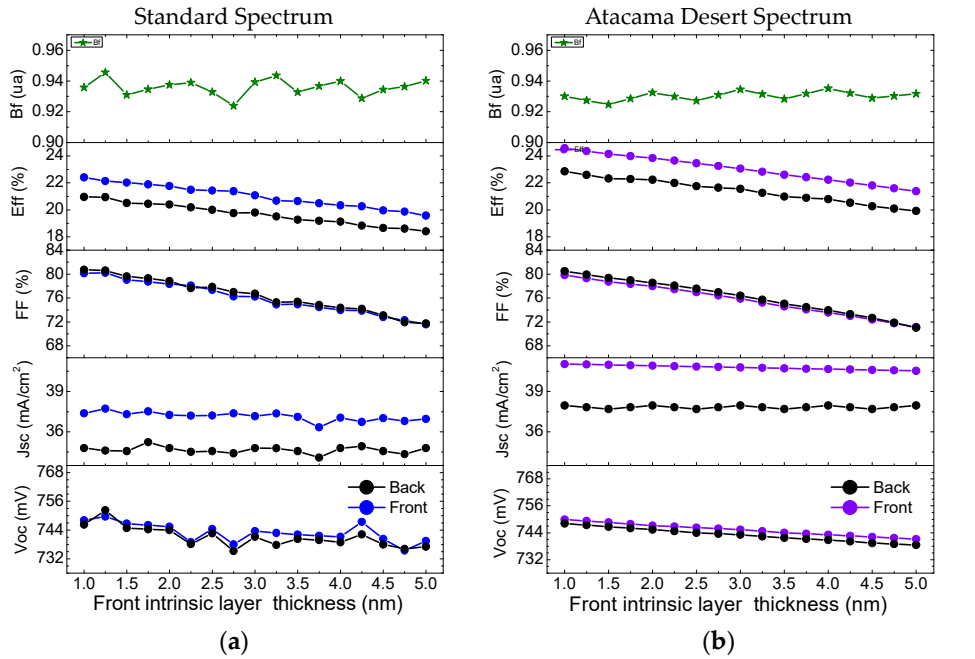

Figure A8. Optimization of $a - Si : H(i)$, located at the front part of the solar cell, according to thickness. (**a**) The black line shows bifaciality and IV values when the light strikes the back part, while the blue line shows these values when the light strikes the front part, with the AM1.5 standard spectrum. (**b**) The black line shows bifaciality and IV values when the light strikes from the back part, while the violet line shows these values when the light strikes from the front part, with the Atacama Desert solar spectrum.

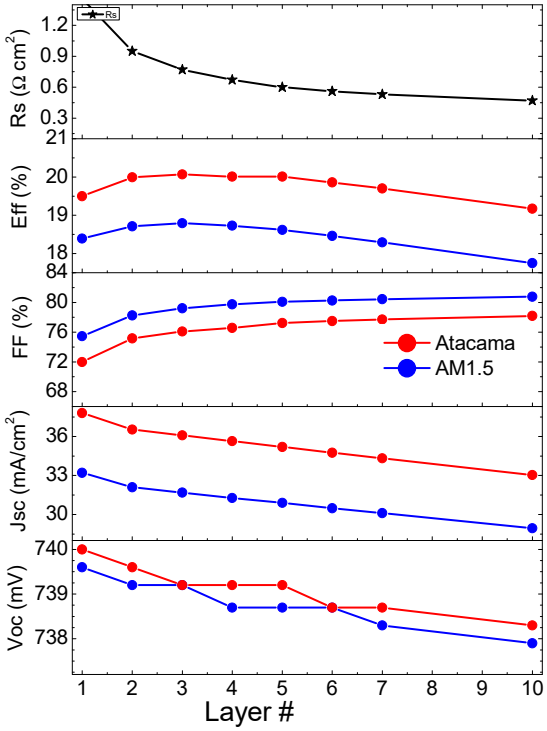

Figure A9. 16. Solar cell optimization. Varying the number of graphene layers on the front part as a transparent conductive electrode. The red line shows the Atacama spectrum values, while the blue line shows the AM1.5 standard spectrum values.

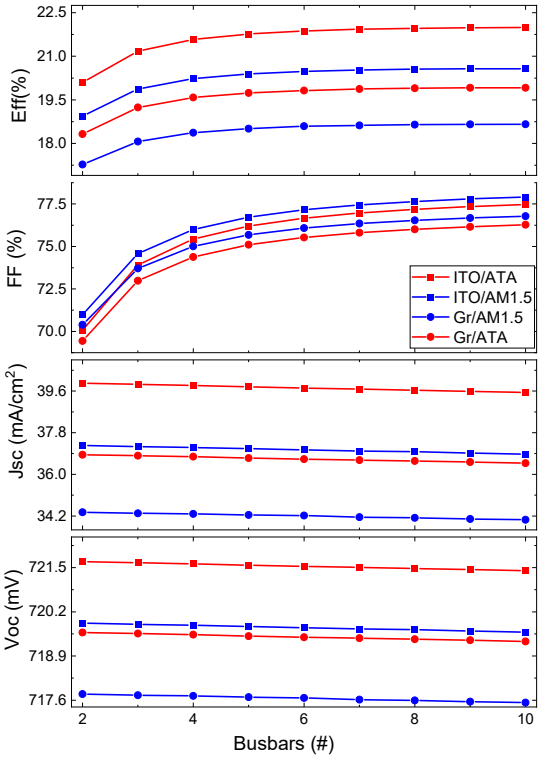

Figure A10. Varying the number of busbars. The red line shows the Atacama Desert spectrum values, while the blue line shows the AM1.5 standard spectrum values. The squares shows ITO values while the circles shows graphene values.

Table A1. Photovoltaic parameters computed in this work and obtained from related references.

TCL	V_{oc} [mV]	J_{sc} [mA/cm^2]	*FF* [%]	*Eff* [%]	Ref.
ITO	761.9	37.19	76.88	21.78	This work
3-layer graphene	739.2	31.68	79.2	18.79	This work
ITO	713	37.3	75.9	20.2	[63]
ITO	689	15.6	57.2	6.1	[15]
1-layer graphene + Ni-grid	638	12.7	51.9	4.2	[15]
AZO	657	32.1	72.1	15.21	[21]
4-layer graphene	601	25.5	64	9.81	[21]

References

1. Yoshikawa, K.; Kawasaki, H.; Yoshida, W.; Irie, T.; Konishi, K.; Nakano, K.; Uto, T.; Adachi, D.; Kanematsu, M.; Uzu, H.; et al. Silicon heterojunction solar cell with interdigitated back contacts for a photoconversion efficiency over 26%. *Nat. Energy* **2017**, *2*, 17032. [CrossRef]
2. De Wolf, S.; Descoeudres, A.; Holman, Z.C.; Ballif, C. High-efficiency Silicon Heterojunction Solar Cells: A Review. *Green* **2012**, *2*, 7–24. [CrossRef]
3. Tiwari, P.; Patel, K.; Krishnia, L.; Kumari, R.; Tyagi, P.K. Potential application of multilayer n-type tungsten diselenide (WSe 2-sheet as transparent conducting electrode in silicon heterojunction solar cell. *Comput. Mater. Sci.* **2017**, *136*, 102–108. [CrossRef]
4. Yu, Y.; Zhao, Y.; Ryu, S.; Brus, L.S.; Kim, K.S.; Kim, P. Tuning the Graphene Work Function by Electric Field Effect. *Nano Lett.* **2009**, *9*, 3430–3434. [CrossRef] [PubMed]
5. Li, B.X.; Zhu, H.; Wang, K.; Cao, A.; Wei, J.; Li, C. Graphene-On-Silicon Schottky Junction Solar Cells. *Adv. Mater.* **2010**, *22*, 2743–2748. [CrossRef] [PubMed]
6. Khrapach, I.; Withers, F.; Bointon, T.H.; Polyushkin, D.K.; Barnes, W.L.; Russo, S.; Craciun, M.F. Novel Highly Conductive and Transparent Graphene-Based Conductors. *Adv. Mater.* **2012**, *24*, 2844–2849. [CrossRef]
7. Aasi, A.; Ebrahimi Bajgani, S.; Panchapakesan, B. A first-principles investigation on the adsorption of octanal and nonanal molecules with decorated monolayer WS promising gas sensing platform. *AIP Adv.* **2023**, *13*, 025157. [CrossRef]
8. Baig, N. Two-dimensional nanomaterials: A critical review of recent progress, properties, applications, and future directions. *Compos. Part A Appl. Sci. Manuf.* **2023**, *165*, 107362. [CrossRef]
9. Qin, F.; Chen, J.; Liu, J.; Liu, L.; Tang, C.; Tang, B.; Li, G.; Zeng, L.; Li, H.; Yi, Z. Design of high efficiency perovskite solar cells based on inorganic and organic undoped double hole layer. *Sol. Energy* **2023**, *262*, 111796. [CrossRef]
10. Hora, C.; Santos, F.; Pereira, A.M.; Sales MG, F.; Ivanou, D.; Mendes, A. PEDOT-graphene counter-electrode for solar and improved artificial light conversion in regular, bifacial and FTO-less cobalt mediated DSSCs. *Electrochim. Acta* **2022**, *412*, 140140. [CrossRef]
11. Lai, R.; Shi, P.; Yi, Z.; Li, H.; Yi, Y. Triple-Band Surface Plasmon Resonance Metamaterial Absorber Based on Open-Ended Prohibited Sign Type Monolayer Graphene. *Micromachines* **2023**, *14*, 953. [CrossRef]
12. Tang, B. Polarization-controlled and symmetry-dependent multiple plasmon-induced transparency in graphene-based metasurfaces. *Opt. Express* **2022**, *30*, 35554–35566. [CrossRef] [PubMed]
13. Ochoa-Martínez, E.; Gabás, M.; Barrutia, L.; Pesquera, A.; Centeno, A.; Palanco, S.; Zurutuza, A.; Algora, C. Determination of a refractive index and an extinction coefficient of standard production of CVD-graphene. *Nanoscale* **2015**, *7*, 1491–1500. [CrossRef]
14. Lee, H.C.; Liu, W.; Chai, S.; Mohamed, R. Review of the synthesis, transfer, characterization and growth mechanisms of single and multilayer graphene. *RSC Adv.* **2017**, *7*, 15644–15693. [CrossRef]
15. Dianetti, M.; Susanna, G.; Calabrò, E.; Polino, G.; Otto, M.; Neumaier, D.; Reale, A.; Brunetti, F. Graphene with Ni-Grid as Semitransparent Electrode for Bulk Heterojunction Solar Cells (BHJ-SCs). *Polymers* **2022**, *14*, 1046. [CrossRef] [PubMed]
16. Bae, S.; Kim, K.; Lee, Y.; Xu, X.; Park, J.; Zheng, Y. Roll-to-roll production of 30-inch graphene films for transparent electrodes. *Nat. Nanotechnol.* **2011**, *5*, 574–578. [CrossRef]
17. Vaianella, F.; Rosolen, G.; Maes, B. Graphene as a transparent electrode for amorphous silicon-based solar cells. *J. Appl. Phys.* **2015**, *117*, 243102. [CrossRef]
18. Wen, X.; Zeng, X.; Liao, W.; Lei, Q.; Yin, S. An approach for improving the carriers transport properties of a-Si: H/c-Si heterojunction solar cells with efficiency of more than 27%. *Sol. Energy* **2013**, *96*, 168–176. [CrossRef]
19. Jošt, M.; Kegelmann, L.; Korte, L.; Albrecht, S. Monolithic Perovskite Tandem Solar Cells: A Review of the Present Status and Advanced Characterization Methods Toward 30% Efficiency. *Adv. Energy Mater.* **2020**, *10*, 1904102.
20. Foroughi, J.; Antiohos, D.; Wallace, G.G. Effect of post-spinning on the electrical and electrochemical properties of wet spun graphene fibre. *RSC Adv.* **2017**, *6*, 46427–46432. [CrossRef]

21. Lancellotti, L.; Bobeico, E.; Della Noce, M.; Mercaldo, L.V.; Usatii, I.; Veneri, P.D.; Bianco, G.V.; Sacchetti, A.; Bruno, G. Graphene as non conventional transparent conductive electrode in silicon heterojunction solar cells. *Appl. Surf. Sci.* **2020**, *525*, 146443. [CrossRef]
22. Torres, I.; Fernández, S.; Fernández-Vallejo, M.; Arnedo, I.; Gandía, J.J. Graphene-based electrodes for silicon heterojunction solar cell technology. *Materials* **2021**, *14*, 4833. [CrossRef] [PubMed]
23. Morales, A.; Hernández, N.; Casados, G. Modeling solar cells: A method for improving their efficiency. *Mater. Sci. Eng. B* **2012**, *177*, 1430–1435. [CrossRef]
24. Hernandez, N.; Morales, A. Simulation of heterojunction silicon solar cells with AMPS-1D. *Sol. Energy Mater. Sol. Cells* **2010**, *94*, 62–67. [CrossRef]
25. Qin, L.; Xiao, Y.; Cheng, L.; Ming, C. Performance of bifacial HIT solar cells on n-type silicon substrates. *Optoelectron. Lett.* **2010**, *6*, 108–111.
26. Patel, K.; Tyagi, P.K. Multilayer graphene as a transparent conducting electrode in silicon heterojunction solar cells. *AIP Adv.* **2015**, *5*, 077165. [CrossRef]
27. Patel, K.; Tyagi, P.K. P-type multilayer graphene as a highly efficient transparent conducting electrode in silicon heterojunction solar cells. *Carbon* **2017**, *116*, 744–752. [CrossRef]
28. Wilbert, S.; Jessen, W.; Gueymard, C.A.; Polo, J.; Bian, Z.; Driesse, A.; Habte, A.; Marzo, A.; Armstrong, P.; Vignola, F.; et al. Proposal and Evaluation of Subordinate Standard Solar Irradiance Spectra with a Focus on Air Mass Effects. In Proceedings of the ISES Solar World Congress 2017 and IEA SHC Solar Heating and Cooling Conference for Buildings and Industry 2017, Abu Dhabi, United Arab Emirates, 29 October–2 November 2017; pp. 1372–1384. [CrossRef]
29. Jessen, W.; Wilbert, S.; Gueymard, C.A.; Polo, J.; Bian, Z.; Driesse, A.; Habte, A.; Marzo, A.; Armstrong, P.; Vignola, F.; et al. Evaluation of Subordinate Standard Solar Irradiance Spectra for Applications in Solar Energy Systems. *Sol. Energy* **2018**, *168*, 30–43. [CrossRef]
30. Zhao, Y.; Xue, P.; Fan, C.; Li, B.; Zhang, N.; Ma, T.; Xie, J.; Liu, J. Data mining techniques for novel local reference solar irradiance spectra calculations: A case study in Beijing. *Sol. Energy* **2023**, *258*, 106–117. [CrossRef]
31. Gueymard, C.A.; Myers, D.; Emery, K. Proposed reference irradiance spectra for solar energy systems testing. *Sol. Energy* **2002**, *73*, 443–467. [CrossRef]
32. Marzo, A.; Polo, J.; Wilbert, S.; Gueymard, C.A.; Jessen, W.; Ferrada, P.; Alonso-Montesinos, J.; Ballestrín, J. Sunbelt spectra comparison with standard ASTM G173: The Chilean case. In *AIP Conference Proceedings*; AIP Publishing LLC: Melville, NY, USA, 2018; p. 190010. [CrossRef]
33. Marzo, A.; Ferrada, P.; Beiza, F.; Alonso-Montesinos, J.; Ballestrín, J.; Román, R. Comparison of Atacama Desert Solar Spec-trum vs. ASTM G173-03 Reference Spectra for Solar Energy Applications. In Proceedings of the 11th International Solar Energy Society (ISES) EUROSUN Conference, Palma de Mallorca, Spain, 11–14 October 2016.
34. Marzo, A.; Ferrada, P.; Beiza, F.; Besson, P.; Montesinos, J.A.; Ballestrín, J.; Román, R.; Portillo, C.; Escobar, R.; Fuentealba, E. Standard or local solar spectrum Implications for solar technologies studies in the Atacama Desert. *Renew. Energy* **2018**, *127*, 871–882. [CrossRef]
35. Kato, S.; Rose, F.G.; Sun-Mack, S.; Miller, W.F.; Chen, Y.; Rutan, D.A.; Stephens, G.L.; Loeb, N.G.; Minnis, P.; Wielicki, B.A.; et al. Improvements of top-of-atmosphere and surface irradiance computations with CALIPSO-, CloudSat-, and MODIS-derived cloud and aerosol properties. *J. Geophys. Res. Atmos.* **2011**, *116*, 1–21. [CrossRef]
36. Remer, L.A.; Kaufman, Y.J.; Tanré, D.; Mattoo, S. The MODIS Aerosol Algorithm, Products, and Validation. *J. Atmos. Sci.* **2005**, *62*, 947–973. [CrossRef]
37. Wang, H.; Zou, X.; Li, G. An Improved Quality Control for AIRS Total Column Ozone Observations within and around Hurricanes. *J. Atmos. Ocean. Technol.* **2012**, *29*, 417–432. [CrossRef]
38. ECMWF | ERA Interim, Daily, 2022. Available online: https://apps.ecmwf.int/datasets/data/interim-full-daily/levtype=sfc/ (accessed on 12 April 2022).
39. Gueymard, C.A. Parameterized transmittance model for direct beam and circumsolar spectral irradiance. *Sol. Energy* **2001**, *71*, 325–346. [CrossRef]
40. Giovanni. 2022. Available online: https://giovanni.gsfc.nasa.gov/giovanni/ (accessed on 12 April 2022).
41. Gueymard, C. SMARTS: Simple Model of the Atmospheric Radiative Transfer of Sunshine | Grid Modernization | NREL. 1995. Available online: https://www.nrel.gov/grid/solar-resource/smarts.html (accessed on 23 March 2019).
42. Weber, J.W.; Calado, V.E.; Van De Sanden, M.C.M. Optical constants of graphene measured by spectroscopic ellipsometry. *Appl. Phys. Lett.* **2010**, *97*, 091904. [CrossRef]
43. Available online: https://refractiveindex.info/?shelf=main&book=C&page=Weber (accessed on 1 June 2023).
44. Dahshan, A.; Aly, K.A. Determination of the thickness and optical constants of amorphous Ge-Se-Bi thin films. *Philos. Mag.* **2009**, *89*, 1005–1016. [CrossRef]
45. Birgin, E.G.; Chambouleyron, I.; Mario Martínez, J. Estimation of the optical constants and the thickness of thin films using unconstrained optimization. *J. Comput. Phys.* **1999**, *151*, 862–880. [CrossRef]
46. van Sark, W.; Korte, L.; Roca, F. (Eds.) *Physics and Technology of Amorphous-Crystalline Heterostructure Silicon Solar Cells*; Springer: Berlin/Heidelberg, Germany, 1981; p. 53.

47. Lachenal, D.; Baetzner, D.; Frammelsberger, W.; Legradic, B.; Meixenberger, J.; Papet, P.; Strahm, B.; Wahli, G. Heterojunction and Passivated Contacts: A Simple Method to Extract Both n/tco and p/tco Contacts Resistivity. *Energy Procedia* **2016**, *92*, 932–938. [CrossRef]
48. Coignus, J.; Baudrit, M.; Singer, J.; Lachaume, R.; Muñoz, D.; Thony, P. Key issues for accurate simulation of a-Si: H/c-Si heterojunction solar cells. *Energy Procedia* **2011**, *8*, 174–179. [CrossRef]
49. Dongo, P.D.; Kapim, A.D.; Pelap, F.B. Effects of a Thermal Nonlinear Resistance on the Power Output of the PV Cell. *J. Energy Technol. Policy* **2014**, *4*, 100–111.
50. Kim, H.-Y.; Dawood, O.M.; Monteverde, U.; Sexton, J.; Li, Z.; Britnell, L.; Migliorato, M.A.; Young, R.J.; Missous, M. Multilayer stacking and metal deposition effects on large area graphene on GaAs. *Carbon* **2016**, *96*, 83–90. [CrossRef]
51. Lim, E.L.; Yap, C.C.; Jumali, M.H.H.; Teridi, M.A.M.; Teh, C.H. A Mini Review: Can Graphene Be a Novel Material for Perovskite Solar Cell Applications? *Nano Micro Lett.* **2018**, *10*, 1–12. [CrossRef] [PubMed]
52. Negishi, R.; Wei, C.; Yao, Y.; Ogawa, Y.; Akabori, M.; Kanai, Y.; Matsumoto, K.; Taniyasu, Y.; Kobayashi, Y. Turbostratic Stacking Effect in Multilayer Graphene on the Electrical Transport Properties. Phys. *Status Solidi Basic Res.* **2020**, *257*, 1900437. [CrossRef]
53. Park, M.; Kim, J.; Song, H.; Kim, S.; Jeon, M. Fast and stable ionic electroactive polymer actuators with PEDOT:PSS/(graphene–Ag-Nanowires) nanocomposite electrodes. *Sensors* **2018**, *18*, 11–15. [CrossRef]
54. Liu, G.; Rumyantsev, S.; Shur, M.S.; Balandin, A.A. Origin of 1/f noise in graphene multilayers: Surface vs. volume. *Appl. Phys. Lett.* **2013**, *102*, 093111. [CrossRef]
55. Paquin, F.; Rivnay, J.; Salleo, A.; Stingelin, N.; Silva, C. Multi-phase semicrystalline microstructures drive exciton dissociation in neat plastic semiconductors. *J. Mater. Chem. C* **2015**, *3*, 10715–10722. [CrossRef]
56. Grande, M.; Bianco, G.V.; Vincenti, M.A.; de Ceglia, D.; Capezzuto, P.; Scalora, M.; D'Orazio, A.; Bruno, G. Optically Transparent Microwave Polarizer Based on Quasi-Metallic Graphene. *Sci. Rep.* **2015**, *5*, 17083. [CrossRef]
57. Chan, S.H.; Chen, S.H.; Lin, W.T.; Kuo, C.C. Uniformly distributed graphene domain grows on standing copper via low-pressure chemical vapor deposition. *Adv. Mater. Sci. Eng.* **2013**, *2013*, 460732. [CrossRef]
58. Bianco, G.V.; Sacchetti, A.; Milella, A.; Grande, M.; D'Orazio, A.; Capezzuto, P.; Bruno, G. Extraordinary low sheet resistance of CVD graphene by thionyl chloride chemical doping. *Carbon* **2020**, *170*, 75–84. [CrossRef]
59. Sun, H.; Ge, G.; Zhu, J.; Yan, H.; Lu, Y.; Wu, Y.; Wan, J.; Han, M.; Luo, Y. High electrical conductivity of graphene-based transparent conductive films with silver nanocomposites. *RSC Adv.* **2015**, *5*, 108044–108049. [CrossRef]
60. Hendrichs, M.; Padilla, M.; Walter, J.; Clement, F.; Rech, B. Screen-Printed Metallization Concepts for Large-Area Back-Contact Back-Junction Silicon Solar Cells. *IEEE J. Photovolt.* **2016**, *6*, 374–383. [CrossRef]
61. Braun, S.; Hahn, G.; Nissler, R.; Pönisch, C.; Habermann, D. The Multi-Busbar Design: An Overview. *Energy Procedia* **2013**, *43*, 86–92. [CrossRef]
62. Jouini, A.; Ponthenier, D.; Lignier, H.; Enjalbert, N.; Marie, B.; Drevet, B.; Pihan, E.; Cayron, C.; Lafford, T.; Camel, D. Improved Multicrystalline Silicon Ingot Crystal Quality through Seed Growth for High Efficiency Solar Cells: Improved Mc-Si Ingot Crystal Quality through Seed Growth. *Prog. Photovolt. Res. Appl.* **2012**, *20*, 735–746. [CrossRef]
63. Jay, F.; Muñoz, D.; Desrues, T.; Pihan, E.; de Oliveira, A.; Enjalbert, N.; Jouini, A. Advanced Process for N-Type Mono-like Silicon a-Si:H/c-Si Heterojunction Solar Cells with 21.5% Efficiency. *Sol. Energy Mater. Sol. Cells* **2014**, *130*, 690–695. [CrossRef]
64. Available online: https://www.pvlighthouse.com.au/ (accessed on 1 July 2023).